

INVESTIGATING DISTANCE-DEPENDENT DISTORTION IN MULTIMEDIA PHOTOGRAMMETRY FOR FLAT REFRACTIVE INTERFACES

Robin Rofallski*, Oliver Kahmen, Thomas Luhmann

Institute for Applied Photogrammetry and Geoinformatics, Jade University of Applied Sciences, Oldenburg, Germany
(robin.rofallski, oliver.kahmen, thomas.luhmann)@jade-hs.de

Technical Commission II

KEY WORDS: Underwater Photogrammetry, Bundle Adjustment, Ray Tracing, Camera Calibration, Flat Port, Simulation

ABSTRACT:

Multimedia camera calibration is a challenging, yet increasingly important task. Due to the lack of software with appropriate models, implicit calibrations with standard single-media models are often performed, despite the well-known fact that distance-dependent errors arise from neglecting the specific multimedia influences. This becomes particularly relevant when test field calibrations are employed. We present a thorough simulation approach that shows the influence of distance-dependent errors when performing implicit calibration. Results show major accuracy decreases for performing measurements far from the calibration distance while closer distances may compensate the errors quite well. Furthermore, we investigate on the behavior of different test field geometries and angles between interface and optical axis which particularly affects the achievable accuracy.

1. INTRODUCTION

Multimedia photogrammetry has evolved to an important and widely-used means for many applications, such as construction inspection (Hover et al., 2012; Kahmen and Luhmann, 2022), marine habitat monitoring (Marre et al., 2019), wreck surveying (Prado et al., 2019; Rofallski et al., 2020), optical navigation (Johnson-Roberson et al., 2010; Servos et al., 2013) or fluid dynamics (Maas, 1995).

For underwater photogrammetry, cameras are generally placed in a waterproof housing viewing through a clear interface into the water. For the interface, either planar (flat) or hemispherical (dome) ports are used. Dome ports, aligned concentrically with the entry pupil of the lens, allow for mitigation of many image degrading aberrations, including refraction. However, dome alignment still remains a challenging task as the entry pupil is generally non-tangible and varies with focal length, focus distance and lens design (Menna et al., 2016).

Distinct challenges with underwater imagery on the one hand include reduced image quality due to chromatic aberration, dispersion, turbidity and color shift towards blue and green (Maas, 2015). On the other hand, the geometric image formation model is changed due to refraction occurring at different media intersections in the ray path. This generally renders the pinhole model invalid if no distinct shapes of interfaces (i.e. well-centered dome ports) are used, introducing distance-dependent systematic errors when neglecting refractive effects (Treibitz et al., 2012).

Compensation for refraction in the optical ray path with flat ports can be performed either explicitly by calibrating refractive media with their shape, position, orientation and refractive properties or implicitly by partly absorbing refraction effects using pinhole models with additional parameters (Shortis, 2015). Since most publicly available software packages (both commercial and open-source) do not provide any explicit

calibration models, implicit calibration is still widely performed and resulting errors have to be accepted. However, the magnitude of the implicit approach's errors is dependent on several parameters, such as the orientation and position of refractive interfaces and refractive indices of the media. Often, cameras are calibrated in a laboratory or water tank beforehand, as self-calibration in situ may fail due to limited variation in acquisition geometry or little object structure. Hence, differences between calibration and acquisition distance introduce errors to the bundle when neglecting refraction, as stated by Kahmen et al. (2020).

In this contribution, the distance-dependent distortion in multimedia photogrammetry is evaluated for a variety of different calibration distances, assuming a test field calibration. The so calibrated interior orientation parameters are then introduced to bundles with different scaling of object space to obtain errors in object space. We use both the implicit compensation with the Brown model, including three sets of distortion parameters (Brown, 1971) and an explicit ray tracing approach, according to Rofallski and Luhmann (2022).

This paper outlines as follows: After a review on related work regarding multimedia photogrammetry and investigations on implicit calibration, the basic data set and simulation procedure is illustrated. Then, influencing parameters are varied to show the effects of the specific parameter. Eventually, noise is exemplarily added to the data. Results are discussed and findings depicted to provide a theoretical guideline on the subject in the conclusion.

2. RELATED WORK

As the general pinhole model is rendered invalid, alternative projection functions were developed over the years. This includes extended pinhole camera models with additional parameters to correct distortions directly (Maas, 1995; Elnashef and Filin, 2019; Nocerino et al., 2021), extensions to non-single viewpoint cameras (Agrawal et al., 2012; Treibitz et al.,

* Corresponding author

2012) or virtually shifted cameras (Telem and Filin, 2010; Jordt-Sedlazeck and Koch, 2012). Kotowski (1987) introduced a fully flexible but computationally very expensive ray tracing bundle adjustment to account for refraction. Here, all image points are described as vectors that are refracted at each media intersection. The major advantage of this approach is complete control over all refracting interfaces in the ray path which can explicitly be calibrated in the bundle adjustment. Extensions regarding the integration to bundle adjustment and optimization are given by Mulsow (2010), Mulsow and Maas (2014) and Rofallski and Luhmann (2022).

Kang et al. (2012) discussed the issue of neglecting refraction with varying arrangements of the optical axis and interface plane. The authors investigated underwater imagery (both simulated and real) and adjusted combinations of the camera constant and radial-symmetric distortion on natural feature points. The findings were that for mostly perpendicular arrangements of optical axis and interface, no significant loss of accuracy is present and the given calibration of distortion and camera constant suffice for high accuracy. However, the stated accuracy of 0.7 mm for an object with an extent about 200 mm (equals 1:286 relative accuracy) is well below expectable accuracy in underwater photogrammetry.

Kahmen et al. (2019) focused on stereo data sets and especially considered relative and exterior orientation when neglecting refraction. Especially, a change in the stereo-baseline which results in erroneous scaling of object space, was found which can only partly be compensated by other correlated parameters of exterior and interior orientation. Based on that paper, the authors extended their work in Kahmen et al. (2020) by extensive simulations. The influence of varying acquisition distances was addressed when neglecting refraction for stereo systems. Authors focused their work on orientation parameters mostly and did not include bundle adjustment or deviations from perpendicularity of optical axis and interface.

Rofallski and Luhmann (2022) evaluated a laboratory data set and compared an own ray-tracing-based methodology to ray tracing by Mulsow and Maas (2014) and the Brown model. Results showed a small accuracy decrease of about 10% for a perpendicular setup and a major decrease of 50% for an intersection angle of about 80° with implicit compensation. In Sedlazeck and Koch (2012), the authors thoroughly investigated changes of implicit parameters for both interior and exterior orientation, just as object coordinates by altering the intersection angle of optical axis and interface with synthetically rendered images. The simulations assume self-calibration with natural features for SfM. It is shown that errors in object space occur either radially-symmetric in case of perpendicular setups and more complex shapes and higher magnitude with a slanted setup.

Hemmati and Rashtchi (2019) investigated refraction with varying intersection angles and different glass thicknesses. The average reprojection error was increased by more than 50% when non-perpendicular views through the interface were performed in air. Nocerino et al. (2021) tackled the distance dependence by including a second order polynomial as a distance-dependent correction term to the bundle adjustment and evaluated the method in large-scale simulations.

In extension to these works, our contribution towards the assessment of accuracy and errors for implicit multimedia calibration are investigations on the following subjects:

- Calibration distance vs. measurement distance for test field calibrations with nearly equal geometry
- Test field geometry (2D vs. 3D)
- Variation of the angle between optical axis and interface
- Analysis of object points through full bundle adjustments
- Analysis of both implicit and explicit approaches with simulated noise

3. METHODOLOGY

The methodology is based on the assumption of a test field calibration, consisting of a *calibration stage* where interior orientation parameters (IOP) are determined and a *measurement stage* where determined IOP are fixed to their calibrated values and a bundle adjustment only solves for exterior orientations (EOP) and object coordinates (OP).

Table 1. Setup parameters for both evaluated data sets. d_1 is the distance from the perspective center to the first interface.

Camera constant c	-10 mm
Principal point	$x'_0 = y'_0 = 0$ mm
Distortion parameters	0
μ_{air}	1.00028
μ_{glass}	1.49
μ_{water}	1.3318
d_1	20 mm
Interface thickness	8.42 mm
Image noise σ	0
No. cam. stations	100
No. object points	208
No. image points	8500 (2D)
(approx. per bundle)	17000 (3D)

The original geometry was based on a test field and a semi-spherical set of camera stations, consisting of 25 positions where at each, four rolled images were taken, resulting in 100 camera stations. To maintain comparable acquisition geometry, both EOP and OP were equally scaled to any given radius r of the semi-sphere. Regardless of calibration or measurement stage and the used model for IOP and refraction, all image coordinates were simulated individually with an IOP and refraction setup, as depicted in Table 1. Refractive parameters consisted of orientation parameters for two plane-parallel interfaces and refractive indices (μ_i) for the three involved media, air, glass and water. Definitions followed the descriptions in Rofallski and Luhmann (2022). The provided parameters were used, unless stated otherwise.

We used a planar (2D) and a cuboidal (3D) test field for our evaluations (Figure 1). The dimensions of the test fields hence

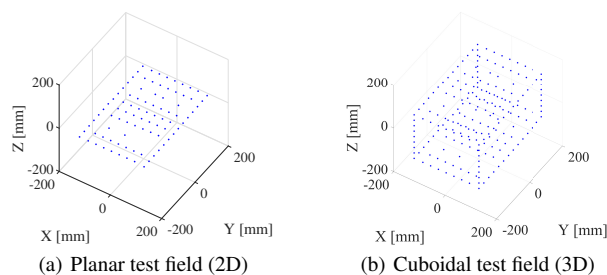


Figure 1. Two test fields for calibration. Additionally, the 3D test field was used for all measurement stage evaluations.

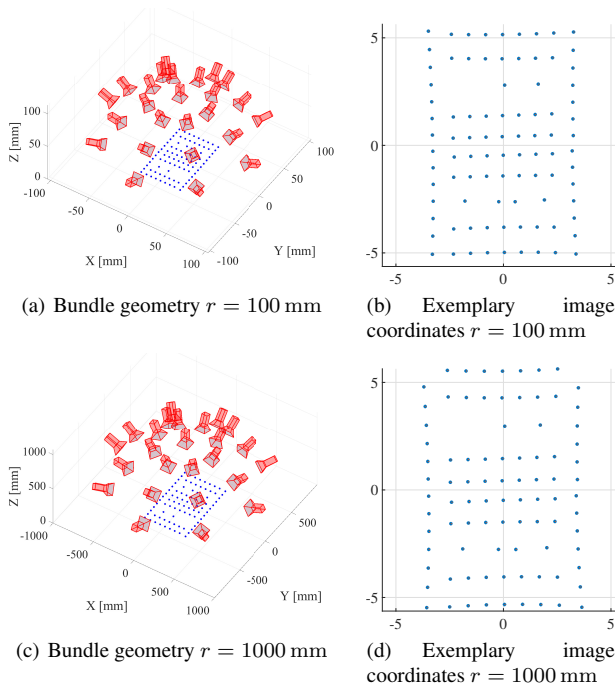


Figure 2. Examples of the bundle geometry and exemplary image coordinates for two different scaling radii r (all units are mm). Mind the disappearing points in the top part in (d).

ranged, analogous to the scaling of the exterior orientations, from $25\text{ mm} \times 40\text{ mm} \times 20\text{ mm}$ for the smallest to $2.5\text{ m} \times 4.0\text{ m} \times 2.0\text{ m}$ for the largest geometry. Regardless of the calibration test field, all bundle data sets at measurement stage were simulated with the cuboid test field which provided a spatial geometry. Scaling was provided by two individual scale constraints for each geometry.

Figure 2 provides an insight on both the bundle geometry and the resulting image coordinates on two exemplary images at different scaling. The image coordinates change non-linearly by small margins due to refraction and introduce the unresolvable distortions for implicit compensation.

For the calibration stage, each configuration was calibrated at an average acquisition distance r (distance to the OP barycenter) of 50, 200, 500, 1000 and 2000 mm with accordingly scaled geometry. Afterwards, each calibrated IOP (including orientation of the interface and refractive index of water for the explicit approach) were fixed to their calibrated values. The subsequent measurement stage consisted of one bundle for each acquisition distance from 50 to 5000 mm in steps of 25 mm with the fixed calibration values, resulting in 200 bundle data sets per calibrated distance and configuration (Figure 3). The image scale, including a factor of 1.3318 for the apparent increase of camera constant, thus ranged from 1:3.75 to 1:375.

For accuracy evaluation, 3D coordinates from each bundle adjustment were transformed through 6DOF transformation onto the scaled reference coordinates that went into the image

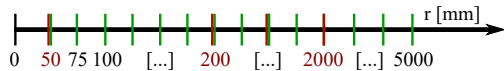


Figure 3. Relation between calibration distances (red) and measurement distances (green)

Table 2. Notations for the different simulated configurations

Interior orientation and refraction	
BRN	Brown model with radial-symmetric and tangential-asymmetric distortion and affinity and shear parameters. All parameters are adjusted.
RTO	Ray tracing in object space, according to Rofallski and Luhmann (2022) with IOP according to Brown. All parameters are adjusted.
XX°	Intersection angle between optical axis and bundle invariant interface plane
Calibration setup	
2D	Calibration is performed with planar test field
3D	Calibration is performed with a cuboidal test field
XXX	Calibration distance. XXX denotes average distance to the test field's barycenter in mm, according to the radius of the used semi-sphere.
σ_X	Image noise, applied to each coordinate component. X is given in fractions of a pixel

coordinate simulation for each given scaling. Resulting RMS_{XYZ} values and relative accuracies (RA: ratio of maximum object extent to RMS_{XYZ} value; Luhmann et al., 2020) were computed. Considering RA has the major advantage of removing image scale which affects all photogrammetric data sets, regardless of the medium. By elimination, effects of refraction become obvious.

Notations regarding the data sets are provided in Table 2. For example, a data set with error-free image coordinates, calibrated at 500 mm distance on the cuboid test field with the Brown model and perpendicular arrangement of optical axis and the planar interface would be named **BRN_2D_500_σ0_90°**.

4. SIMULATIONS WITHOUT NOISE

Several configurations were simulated to show model errors with an implicit approach by using the Brown model with all parameters taking part in the adjustment. We first present results of error-free image coordinates (both calibration and measurement stage) and compare two different calibration test fields; one being planar (2D) and one being cuboidal (3D). Subsequently, we focus on the 3D test field and change the intersection angle of the optical axis and the interface while maintaining error-free image coordinates. We refrain from varying the distance of the interface from the optical center for reasons of readability and complexity.

Eventually, effects of image noise are presented to investigate the relations between image noise and model errors. Additionally, a ray tracing approach by Rofallski and Luhmann (2022) is compared to show results of strict modeling for noisy data. For this entire section, refer to Figure 4, showing absolute RMS values of the transformed coordinates after adjustment (left) and the resulting RA (right).

4.1 Planar and cuboidal test field calibrations

Supporting Figure 4, Table 3 shows accuracy-related parameters of the investigation on 2D and 3D test fields.

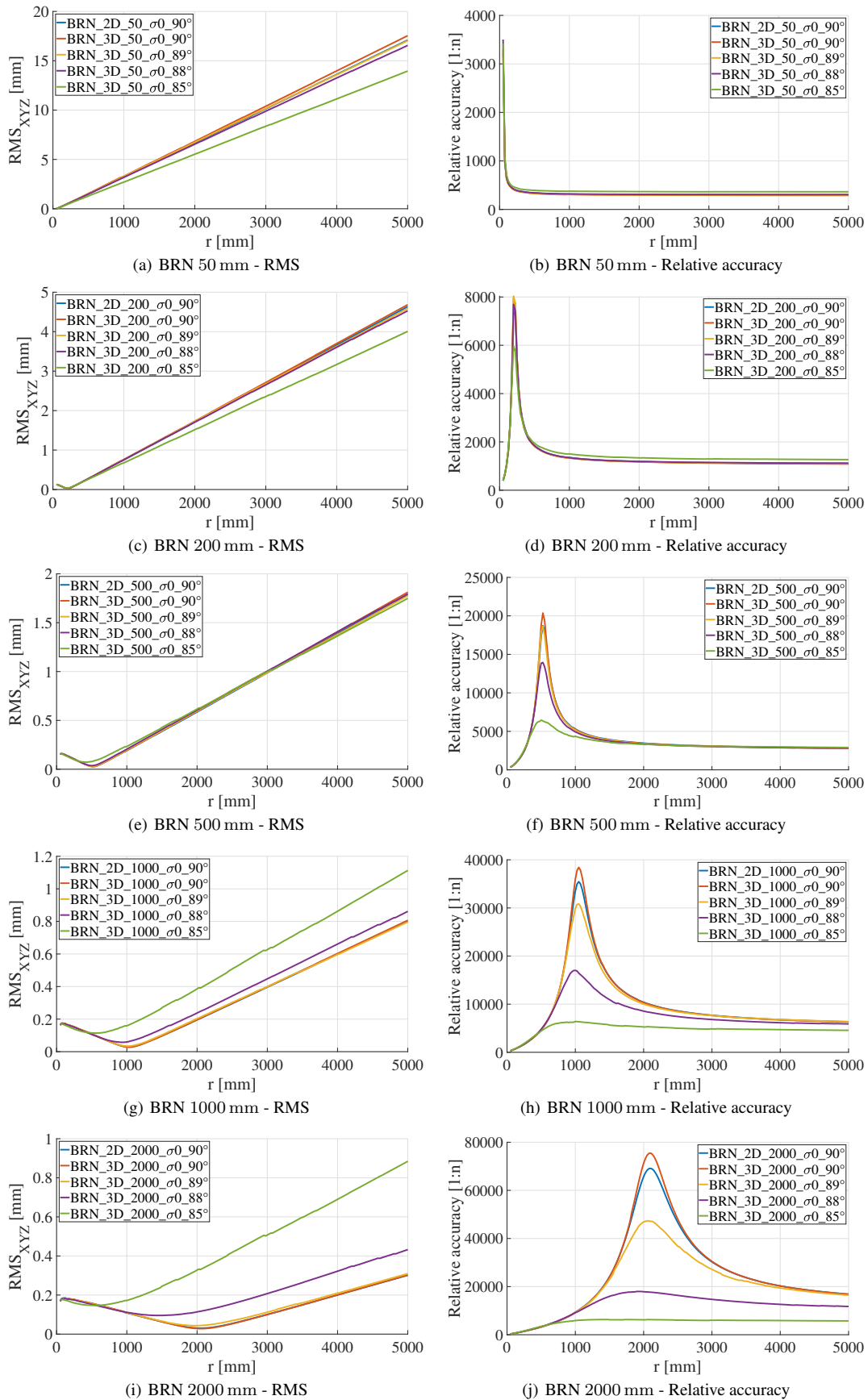


Figure 4. RMS values (left) and relative accuracy (right) of the measurement stage for calibration distances 50 mm, 200 mm, 500 mm, 1000 mm and 2000 mm. All data sets were simulated without image noise and with implicit compensation.

This includes the radius range in which 20 % of the maximum relative accuracy was retained. This is to provide a measure of the width of an accuracy peak, close to the calibration distance and gives an estimate of the depth limits where maximum accuracy for the implicit approach can be anticipated.

Table 3. Min. and max. RMS and relative accuracy (RA) for 2D and 3D data sets. RA \pm 20 % denotes the range of radii where RA remained within 20 % of the max. RA. Note that for curves at 50 mm, a range could not be computed, as the lower end that fell below the given accuracy was not simulated.

	Min RMS [mm]	Max RMS [mm]	Min RA [1:n]	Max RA [1:n]	RA \pm 20 % [mm]
BRN_2D_50.σ0.90°	0.02	17.09	297	3296	-
BRN_2D_200.σ0.90°	0.03	4.63	391	7391	55.6
BRN_2D_500.σ0.90°	0.03	1.79	322	18733	113.3
BRN_2D_1000.σ0.90°	0.03	0.80	304	35458	233.1
BRN_2D_2000.σ0.90°	0.03	0.30	295	69158	469.9
BRN_3D_50.σ0.90°	0.02	17.54	290	3210	-
BRN_3D_200.σ0.90°	0.03	4.68	400	7943	52.10
BRN_3D_500.σ0.90°	0.03	1.81	330	20373	101.6
BRN_3D_1000.σ0.90°	0.03	0.81	311	38439	213.0
BRN_3D_2000.σ0.90°	0.03	0.30	302	75502	424.8

Considering the blue and red lines from Figure 4 which show the results for calibration with the planar (blue) and the cuboidal (red) test field. Generally, a trend towards an accuracy maximum at the calibrated distance, visible in both RMS and relative accuracy for all data sets can be observed. This peak accuracy window was rather small for short distances compared to the longer distances which, by association, had a lower air/water ratio. The window, where 20 % of the maximum relative accuracy was retained, roughly doubled for each distance step. Absolute RMS minima were, among all data sets, rather similar, hence enabling equal maximum absolute accuracy among these data sets. Secondly, after non-linear accuracy convergence towards the maximum below and around the calibration distance, the RMS values increased linearly with distance, as would be the case in a single-media case, too. This can be observed in the relative accuracy as an asymptotic line which all data sets converged to on different levels. The values were close to the shown minimum relative accuracy values. Absolute and relative accuracy rose highest for the longer calibration distances (Figure 4, (j) and entire right column). Lastly, a small accuracy gain was observed for all data sets with the cuboidal test field at a maximum of about 10 %, best visible in Figure 4 (h, j) for 1000 mm and 2000 mm.

4.2 Variation of intersection angle

For all following investigations, only the 3D test field was considered for calibration and the intersection angle between optical axis and interface was varied from the perpendicular setup that was used in the data sets, thus far.

The red, yellow, purple and green lines in Figure 4 show the results for the calibrations with 90°, 89°, 88° and 85° intersection angles, respectively. Supporting the graphics, the same metrics as in the preceding section are shown in Table 4.

Table 4. Values for variation of intersection angle. Refer to Table 3 for further details.

	Min RMS [mm]	Max RMS [mm]	Min RA [1:n]	Max RA [1:n]	RA \pm 20 % [mm]
BRN_3D_50.σ0.89°	0.02	17.03	298	3305	-
BRN_3D_50.σ0.88°	0.01	16.55	306	3502	-
BRN_3D_50.σ0.85°	0.01	13.96	364	3419	-
BRN_3D_200.σ0.89°	0.03	4.59	401	8034	51.6
BRN_3D_200.σ0.88°	0.03	4.53	400	7692	53.3
BRN_3D_200.σ0.85°	0.03	4.01	394	5959	66.2
BRN_3D_500.σ0.89°	0.03	1.78	330	18674	110.6
BRN_3D_500.σ0.88°	0.04	1.79	329	13945	147.7
BRN_3D_500.σ0.85°	0.07	1.75	321	6453	357.1
BRN_3D_1000.σ0.89°	0.03	0.80	311	30837	268.5
BRN_3D_1000.σ0.88°	0.06	0.86	310	17019	425.0
BRN_3D_1000.σ0.85°	0.11	1.11	302	6403	1765.9
BRN_3D_2000.σ0.89°	0.04	0.31	302	47357	681.1
BRN_3D_2000.σ0.88°	0.10	0.43	301	17983	1757.4
BRN_3D_2000.σ0.85°	0.15	0.88	293	6312	-

In general, an accuracy-degrading trend can be observed for all calibration distances when the intersection angle was changed from 90°, showing the optimum for implicit compensation. Especially in the longer calibration distances, this effect was particularly large. However, the 85° data at 50 mm and 200 mm showed a surprising trend towards better accuracy at longer measurement distances whereas the small measurement distances were equally or minimally inferior to other data sets. The higher relative accuracy from 90° data disappears with increasing calibration distance (Figure 4 a,b,c,d). The same also applies to the 88° data set with smaller magnitude. From 500 mm, accuracy for higher deviations from perpendicularity decreased rapidly to considerably poorer values.

The minimum absolute RMS values of 89° were similar to the 90° cases. However, with the lower angles, these minima could not be achieved. Similarly, overall maximum relative accuracy decreased by up to 92 % (2000 mm), compared to 90° cases. The distinct peaks that were visible for perpendicular arrangements, disappear with lower angles, too. This resulted in a rather flat curve for relative accuracy and a shift of the peak for the 85° case towards lower end at approximately 750 mm.

4.3 Discussion

Considering the error-free simulations, we discuss the effects of pure modeling that are shown with the data. Results indicate that accuracy of implicit underwater test field calibration is highly error-prone to deviations from the calibration distance. This behavior however does not propagate unrestricted off the charts but rather converges asymptotically to a horizontal line in relative accuracy space or a linear growth in absolute RMS space. This implies that the effect of refraction, as modeled here, only affects results to a certain distance after which other effects prevail. Especially image measurement accuracy and its

relation to the acquisition distance was not considered for this study. Hence, effects of image degradation and atmospheric variations are to be considered, as well when working on real tasks. Additionally, depth of field is a considerable factor in very close ranges, as is the case with the small distances of 50 mm and 200 mm. The small focal depth strongly reduces image measurement accuracy, especially with spatial test fields. Consequently, the shown small ranges of high accuracy are possibly the only areas that can be imaged in focus and might supersede the long measurement distances for this case.

All accuracy peaks in both RMS and relative accuracy were slightly shifted towards longer distances. This may also be caused by underlying effects of neglected image measurement accuracy which tended to increase relative accuracy towards longer distances when remaining constant. A small accuracy gain towards the cuboidal test field was observed. Since the cuboidal geometry offers a wider depth, the calibration values for this geometry should provide some decorrelation and hence receive the shown higher accuracy with higher peak and a wider range than the 2D calibrations.

The calibration distances of 50, 200, 500, 1000 and 2000 mm relate to air/water ratios of approx. 40/60, 10/90, 4/96, 2/98 and 1/99, respectively. The radii can be transformed to this ratio and results show equal behavior. Hence, the given data does not only apply for the shown calibration and measurement radii but rather for a generalized case with the specific geometry of a semi-shaped sphere and the used test field. Kahmen et al. (2020) found that the refraction effect decreases with higher water percentages water which is also derivable from our data. They considered absolute deviations from spatial intersections, whereas our data shows this for monocular bundle adjustment.

Deviations from perpendicularity showed the higher impact on the accuracy of implicit modeling in our simulations with growing impact towards longer distances. Generally, deviations of 1° could mostly be compensated to a large extent, especially when short calibration and measurement distances were chosen. However, the actual impact can only be assessed by simulation and real data that include image measurement uncertainty as a function of image scale. Higher angle deviations showed larger errors which are most likely not to be compensated by implicit calibration and are in accordance with practical data from Rofallski and Luhmann (2022) or Kahmen et al. (2020).

5. SIMULATIONS WITH NOISE

To assess the influence of image noise, we ran two simulations with added constant noise. Expectable accuracy of 1/20 to 1/50 px on elliptical targets are expected in air (Luhmann et al., 2020). With image degradation, Maas (2015) claims an accuracy loss of factor 5 in multimedia environments. Hence, following the lower bound, we assumed an image measurement accuracy of 1/4 px (1.2 μm) per coordinate direction to be a practically relevant magnitude. Additionally, we used 1 px (4.8 μm) as an error margin for applications with lower accuracy demands which could base on natural features.

Since noisy data produces errors even with correct modeling, we additionally investigated the behavior of an explicit ray tracing (RTO) approach by Rofallski and Luhmann (2022) and compared it to the implicit compensation. The basic principle remained equal to the implicit data sets with a two-step procedure of calibration and introduction of the calibrated values as fixed parameters in the measurement stage.

5.1 Variation of noise

Figure 5 shows the relative accuracy for the 90° case with 3D test field, with the two stated measurement accuracies, included as normally distributed noise to both coordinate directions. With noise of 1/4 px, it can be observed that the smaller calibration distances (50, 200, 500) and their accuracy peaks mostly remained at approximately the same magnitude as in the error-free simulation for the implicit compensation. On the contrary, the longer calibration distances had a reduced accuracy and showed distinctive noisy behavior. The explicitly calibrated bundle indicated a rather noisy behavior but remained constant for almost all data sets over the entire measurement distances. The magnitude was of a comparable magnitude as the 2000 mm data set from the implicit calibration at its peak. Other than that, explicit calibration obtained considerably higher relative accuracies as the implicit approach. A slightly lower accuracy was obtained from the very long calibration distances of RTO (1000 mm and 2000 mm) at short measurement distances which rose to the mean of all data sets at about 10-20 % of their respective calibration distance (best visible in Figure 5 b, bottom left part).

For a noise of 1 px, both implicit and explicit calibrations lost considerable accuracy. The longer calibration distances from implicit calibration obtained an equal peak accuracy and tended closer to the shorter calibration distance's relative accuracies. The ray tracing also showed a large loss in relative accuracy and gained a higher accuracy only for short measurement distances below 1000 mm. Other than that, the accuracy, again, remained constant over the entire measurement range.

5.2 Discussion

All findings from this section are with the caveat that no extensive random sampling was performed and statistical means can differ with larger samples. We therefore refrained from showing any statistical metrics. However, especially for the explicit calibration, the accuracy appears to be widely constant, hence including at least six samples for each noise magnitude with ray tracing calibration.

Within noise, the relative accuracy for the 2000 mm data set reached an equal level, compared to the explicit ray tracing approach around the calibration distance. This rather surprising accuracy is only valid if, on the one hand, image measurement accuracy remains constant over distance. Affected by turbidity and depth of field, this may not be achievable in practical applications. On the other hand, a test field of the given size would have to be manufactured to the required accuracy and be handled under water, in the first place. In our data set, the simulated test field for the 2000 mm data set had a total extent of approximately 1.0 m × 1.5 m × 0.8 m. Furthermore, the range where a comparable accuracy could be obtained, according to our sample, is rather small. With an explicit model, calibration could be performed almost anywhere in the depicted range and accuracy remain constant, within the considered parameters. This may be limited by correlations that can be considerably higher than for in-air models and harder to compute with noisy data (Maas, 2015; Sedlazeck and Koch, 2012). Effects of correlation become apparent in the two longer distances with RTO 1000 and 2000 mm which had a lower accuracy towards the low end. As we discussed already, accuracy for Brown was at longer distances (i.e. higher air-to-water ratios) nearly as good as an explicit compensation. Hence, the entire parameter space can mostly be described

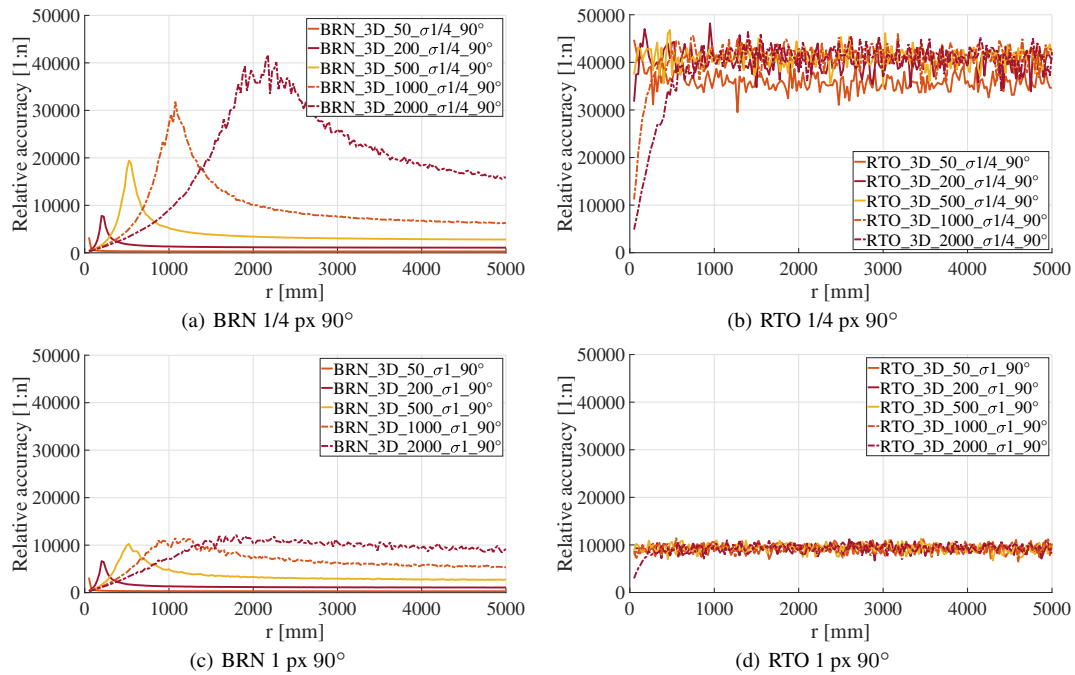


Figure 5. Relative accuracy of noise data of 3D data set with 90° angle (equals combination of red lines in Fig. 4 b, d, f, h, j) for implicit modeling (left) and explicit ray tracing (right). Standard deviation per coordinate was set to $1/4$ px (top) and 1 px (bottom).

without refraction and hence introduces overparametrization and thus large correlations to an explicit approach.

6. CONCLUSION AND OUTLOOK

In this contribution, we provided a theoretical insight on the accuracy assessment of implicit multimedia test field calibration. Through simulations, error-free image coordinates were strictly modeled with refraction and evaluated with an implicit approach by adjusting all distortion parameters of the Brown model. General findings were that the relative accuracy converges towards an asymptotic line, meaning that no unbounded errors arise from unmodeled refraction effects, apart from general accuracy decrease through smaller image scales. Comparisons were performed between 2D and 3D test fields. Differences between the two could be observed but were rather small in magnitude. Secondly, the angle between the optical axis of the camera and the interface plane were altered. Results showed a clear accuracy loss which was considerable from 88° and below. Eventually, erroneous image coordinates were introduced to the simulation and an own ray tracing solution compared to implicit calibration. Results showed a clear advantage for explicit modeling which was expectable.

Generally, the simulations show that implicit test field calibration can be performed, even with little to no accuracy loss, only if many parameters are carefully considered. This includes a close distance to the calibration distance for measurements which can be increased with larger distances (and air-to-water ratios), if image measurement quality remains high enough. Additionally, perpendicularity between optical axis and interface should be maintained. Even small deviations ($>1^\circ$) from this, result in large errors which are very unlikely to be buried in measurement noise.

For future work, a deeper look into correlations and statistics of the impact of noise for implicit calibration should be performed. This especially includes realistic metrics of image measurement

accuracy, e.g. obtained from long term observations through various types of water at different distances. For short ranges, this also includes the depth of field.

The given simulations demanded high computational resources with 200 bundles per calibration distance and configuration, resulting in a total of 7000 bundles. Thus, we refrained from full numerical simulations which would multiply this by the thousands. For full understanding of the noise impact and the expectable residual errors, it would be necessary to perform extensive statistical simulations. Provided the model from Rofallski and Luhmann (2022), this is feasible for a strict ray tracing approach in comparable time as for Brown simulations.

We found that all data could well be described by a second-degree rational function (Figure 6). Despite small outliers at the beginning of the x-range, the coefficient of determination, r^2 as a measure of the goodness of a regression, is in many cases above 0.99, indicating a good fit of the adjusted function (Hughes and Grawoig, 1971). Further investigations are needed to verify or refute this thesis for other data and, if verified, how the coefficients and predictions can be interpreted.

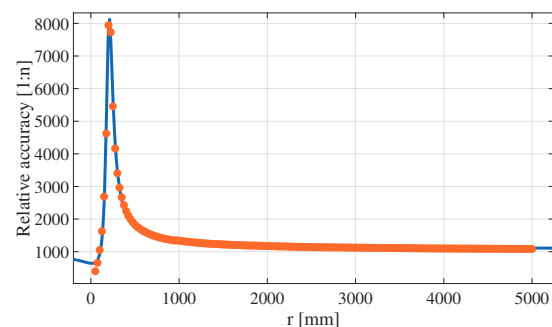


Figure 6. Exemplary data set (orange points) with adjusted second-degree rational function (blue line). $r^2 = 0.9956$

ACKNOWLEDGEMENT

This work was partially supported by German Federal Ministry of Education and Research, funding code 13XP5126C.

REFERENCES

- Agrawal, A., Ramalingam, S., Taguchi, Y., Chari, V., 2012. A theory of multi-layer flat refractive geometry. *IEEE Conf. Comput. Vis. Pattern Recognit.*, 3346–3353.
- Brown, D. C., 1971. Close-Range Camera Calibration. *Photogrammetric Engineering*, 37(8), 855–866.
- Elnashef, B., Filin, S., 2019. Direct linear and refraction-invariant pose estimation and calibration model for underwater imaging. *ISPRS J. Photogramm. Remote Sens.*, 154, 259–271.
- Hemmati, M., Rashtchi, V., 2019. A study on the refractive effect of glass in vision systems. *Int. Conf. Pattern Recognit. Img. Anal.*, IEEE, Piscataway, NJ, 19–25.
- Hover, F. S., Eustice, R. M., Kim, A., Englot, B., Johannsson, H., Kaess, M., Leonard, J. J., 2012. Advanced perception, navigation and planning for autonomous in-water ship hull inspection. *Int. J. Rob. Res.*, 31(12), 1445–1464.
- Hughes, A. J., Grawoig, D., 1971. *Statistics: a foundation for analysis*. Addison-Wesley, Reading.
- Johnson-Roberson, M., Pizarro, O., Williams, S. B., Mahon, I., 2010. Generation and visualization of large-scale three-dimensional reconstructions from underwater robotic surveys. *J. Field Robot.*, 27(1), pp. 21–51.
- Jordt-Sedlazeck, A., Koch, R., 2012. Refractive calibration of underwater cameras. Fitzgibbon A., Lazebnik S., Perona P., Sato Y., Schmid C. (eds), *Lecture Notes in Computer Science*, 7576, Springer, Berlin, Heidelberg, 846–859.
- Kahmen, O., Luhmann, T., 2022. Monocular Photogrammetric System for 3D Reconstruction of Welds in Turbid Water. *PFG – J. Photogramm. Remote Sens. Geoinf. Sci.*
- Kahmen, O., Rofallski, R., Conen, N., Luhmann, T., 2019. On scale definition within calibration of multi-camera systems in multimedia photogrammetry. *Int. Arch. Photogramm. Remote Sens. Spatial Inf. Sci.*, XLII-2/W10, 93–100.
- Kahmen, O., Rofallski, R., Luhmann, T., 2020. Impact of Stereo Camera Calibration to Object Accuracy in Multimedia Photogrammetry. *Remote Sens.*, 12(12), 2057–2087.
- Kang, L., Wu, L., Yang, Y.-H., 2012. Experimental study of the influence of refraction on underwater three-dimensional reconstruction using the SVP camera model. *Appl. Opt.*, 51(31), 7591–7603.
- Kotowski, R., 1987. *Zur Berücksichtigung lichtbrechender Flächen im Strahlenbündel*. Deutsche Geodätische Kommission bei der Bayerischen Akademie der Wissenschaften Reihe C, 330, Beck, München.
- Luhmann, T., Robson, S., Kyle, S., Boehm, J., 2020. *Close-range photogrammetry and 3D imaging*. 3rd edn, De Gruyter, Berlin, Boston.
- Maas, H.-G., 1995. New developments in multimedia photogrammetry. A. Grün, H. Kahmen (eds), *Optical 3D Measurement Techniques III*, Wichmann, Karlsruhe, 362–372.
- Maas, H.-G., 2015. On the Accuracy Potential in Underwater/Multimedia Photogrammetry. *Sensors*, 15(8), 18140–18152.
- Marre, G., Holon, F., Luque, S., Boissery, P., Deter, J., 2019. Monitoring Marine Habitats With Photogrammetry: A Cost-Effective, Accurate, Precise and High-Resolution Reconstruction Method. *Front. Mar. Sci.*, 6.
- Menna, F., Nocerino, E., Fassi, F., Remondino, F., 2016. Geometric and Optic Characterization of a Hemispherical Dome Port for Underwater Photogrammetry. *Sensors*, 16(1), 48–68.
- Mulsow, C., 2010. A flexible multi-media bundle approach. *Int. Arch. Photogramm. Remote Sens. Spatial Inf. Sci.*, XXXVIII/5, 472–477.
- Mulsow, C., Maas, H.-G., 2014. A universal approach for geometric modelling in underwater stereo image processing. *Workshop Comp. Vis. Anal. Underwater Img. (CVAUI)*, 49–56.
- Nocerino, E., Menna, F., Gruen, F., 2021. Bundle Adjustment with Polynomial Point-To-Camera Distance Dependent Corrections for Underwater Photogrammetry. *Int. Arch. Photogramm. Remote Sens. Spatial Inf. Sci.*, XLIII-B2-2021, 673–679.
- Prado, E., Gómez-Ballesteros, M., Cobo, A., Sánchez, F., Rodríguez-Basalo, A., Arrese, B., Rodríguez-Cobo, L., 2019. 3D Modeling of Rio Miera Wreck Ship Merging Optical and Multibeam High Resolution Points Cloud. *Int. Arch. Photogramm. Remote Sens. Spatial Inf. Sci.*, XLII-2/W10, 159–165.
- Rofallski, R., Luhmann, T., 2022. An Efficient Solution to Ray Tracing Problems in Multimedia Photogrammetry for Flat Refractive Interfaces. *PFG – J. Photogramm. Remote Sens. Geoinf. Sci.*
- Rofallski, R., Westfeld, P., Nistad, J.-G., Büttner, A., Luhmann, T., 2020. Fusing ROV-based photogrammetric underwater imagery with multibeam soundings for reconstructing wrecks in turbid waters. *J. Appl. Hydrogr. (116)*, 23–31.
- Sedlazeck, A., Koch, R., 2012. Perspective and non-perspective camera models in underwater imaging – overview and error analysis. *Lecture Notes in Computer Science*, 7474, Springer, Berlin, Heidelberg, 212–242.
- Servos, J., Smart, M., Waslander, S. L., 2013. Underwater stereo slam with refraction correction. *Int. Conf. Intell. Rob. and Sys. (IROS)*, IEEE, Piscataway, NJ, 3350–3355.
- Shortis, M., 2015. Calibration Techniques for Accurate Measurements by Underwater Camera Systems. *Sensors*, 15(12), 30810–30826.
- Telem, G., Filin, S., 2010. Photogrammetric modeling of underwater environments. *ISPRS J. Photogramm. Remote Sens.*, 65(5), 433–444.
- Treibitz, T., Schechner, Y., Kunz, C., Singh, H., 2012. Flat Refractive Geometry. *IEEE Trans. Pattern Anal. Mach. Intell.*, 34(1), 51–65.